Effects of Welding and Weld Heat-Affected Zone Simulation on the Microstructure and Mechanical Behavior of a 2195 Aluminum-Lithium Alloy

D.L. CHEN and M.C. CHATURVEDI

The microstructures, tensile properties, and fatigue properties of a 2195-T8 Al-Li alloy subjected to a weld heat-affected zone (HAZ) simulation and gas-tungsten-arc (GTA) welding using a 4043 filler metal, with and without a postweld heat treatment, were studied. The principal strengthening precipitate in the T8 base alloy was the T_1 (Al_2CuLi) phase. The HAZ simulation resulted in the dissolution of T_1 precipitates and the formation of T_B (Al_7Cu_4Li) phase, Guinier–Preston (G–P) zones, and δ' (Al_3Li) particles. When the HAZ simulation was conducted at the highest temperature of 600 °C, microcracks and voids also formed along the grain boundaries (GBs). In the specimens welded with the 4043 alloy, T (AlLiSi) phase was found to form in the fusion zone (FZ). An elongated T_B phase and microcracks were observed to occur along the GBs in the HAZ close to the FZ interface. The T_1 phase was not observed in the HAZ. The postweld heat treatment resulted in the spheroidization of primary T phase and the precipitation of small secondary T particles in the FZ, the dissolution of T_B phase, and the reprecipitation of the T_1 phase in the HAZ. Both the HAZ simulation and welding gave rise to a considerable decrease in the hardness, tensile properties, and fatigue strength. The hardness in the FZ was lower than that in the HAZ. Although the postweld heat treatment improved both the hardness and tensile properties due to the reprecipitation of T_1 phase in the HAZ and a smaller interparticle spacing in the FZ, no increase in the fatigue strength was observed because of the presence of microcracks in the HAZ.

I. INTRODUCTION

THE aluminum-lithium (Al-Li) alloy 2195 is a candidate material for the next generation of launch vehicles because of its reduced density and improved strength over the 2219 aluminum alloy.[1–4] The effects of composition,[1,5,6] aging conditions,[3,7,8] and processing[4,7,9] on the microstructure and tensile properties of this alloy have been extensively studied, and the high strength and stiffness of the alloy have been attributed primarily to the precipitation of finely distributed T_1 (Al_2CuLi) phase. Since many aerospace applications of the 2195 alloy would involve welding, considerable research efforts have been directed toward studying the weldability[10–16] and weld properties[17–21] of the alloy. These studies have suggested that an improvement in the weld fusion-zone (FZ) integrity can be achieved by modifying the chemistry and microstructure through a proper selection of filler metals and welding parameters, but not the integrity of the heat-affected zone (HAZ). This can be a limiting factor in determining the joint efficiency and, thus, the application of this alloy. Thermal cycles experienced in the HAZ can result in a considerable change in microstructures and degradation in mechanical properties.[17,20,21] The microstructures within the HAZ produced by laser-beam welding,[17,20] variable-polarity plasma arc welding,[20] gas-tungsten-arc (GTA) welding,[17] and friction stir welding[16,18] have been evaluated. Although the microstructure of the HAZ can be characterized by examining actual welds, it is often more convenient and effective to analyze specimens with a microstructure produced by HAZ simulation.[22] Although the microhardness,[17] yield strength,[20] fracture toughness,[19] and corrosion behavior[23] of the welded joints have been reported, the data on the mechanical properties of the HAZ are very limited. In particular, the fatigue behavior of the HAZ and welded joints of the 2195 alloy has not been reported in the open literature.

The objective of this investigation was, therefore, to study the influence of HAZ simulation and welding, with and without a postweld heat treatment, on the microstructures, tensile properties, and fatigue behavior of the 2195-T8 Al-Li alloy.

II. MATERIAL AND EXPERIMENTAL PROCEDURES

The 2195-T8 Al-Li alloy, with a composition of 3.98Cu, 0.96Li, 0.36Mg, 0.28Ag, 0.15Zr, and the balance Al (wt pct), was obtained from Reynolds Metals Company (Chester, VA) in the form of an 8-mm-thick plate.

The HAZ simulation was carried out in a Gleeble 1500 system. Specimens of 130 mm in length and 8 mm in diameter were used. The specimen and the gripping arrangement are shown in Figure 1. The separation between the copper grips was approximately 40 mm. The temperature was measured and controlled through a thermocouple spot welded at the midpoint of the specimen. The specimens were heated at a rate of 300 °C/per second to temperatures between 400

D.L. CHEN, formerly Research Associate, Department of Mechanical and Industrial Engineering, University of Manitoba, is Assistant Professor, Department of Mechanical, Aerospace and Industrial Engineering, Ryerson University, Toronto, ON, Canada M5B 2K3. M.C. CHATURVEDI, FASM, Professor, is with the Department of Mechanical and Industrial Engineering, University of Manitoba, Winnipeg, MB, Canada R3T 5V6.

Manuscript submitted August 28, 2000.

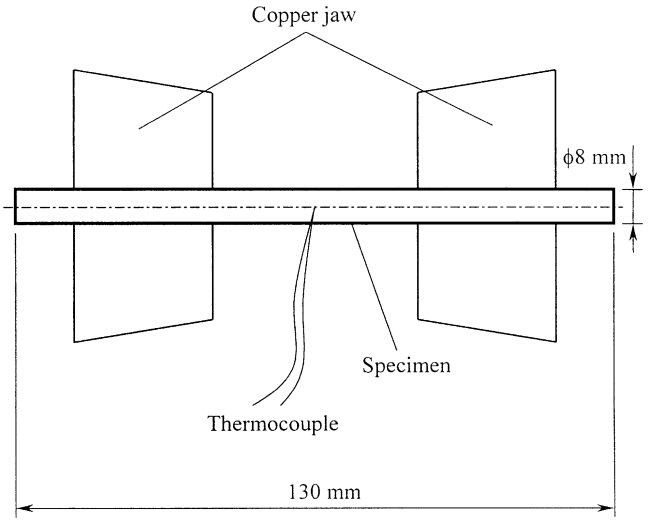

Fig. 1—Gripping arrangement for specimens during HAZ simulation in the Gleeble 1500 system.

°C and 600 °C, followed by a holding time of 3 seconds, then cooled by compressed helium to room temperature.

Gas-tungsten-arc welding was used to join the work pieces with a symmetrical double-V-groove joint geometry. Four passes were performed by using a 4043 filler alloy of 1.6 mm in diameter (first and second passes) and of 3.2 mm in diameter (third and fourth passes). The 4043 filler metal has a chemical composition of 4.5 to 6.0Si, 0.80Fe, 0.30Cu, 0.20Ti, 0.10Zn, 0.05Mn, 0.05Mg, and the remainder Al (wt pct). Welding was conducted in a direction transverse to the plate rolling direction, using 100 A, 12 to 16 V, and a travel speed of about 100 mm per minute. After welding, the workpiece was cut into small pieces, which were used to machine the test specimens with and without the postweld heat treatment. The postweld heat treatment involved a solution treatment (504 °C for 1 hour and water quenched (WQ)) and artificial aging (180 °C for 10 hours and air cooled (AC)).

Microstructures and textures were characterized by optical metallography, image analysis, electron-backscatter diffraction (EBSD)–based orientation imaging microscopy (OIM), X-ray diffraction, electron microscopy using a JEOL*-840 and JSM-5900LV scanning electron microscope (SEM)/energy-dispersive spectrometer (EDS) and a JEM-2000 FX transmission electron microscope (TEM). The TEM thin foils were prepared by the double-jet polishing technique using Struers Tenupol-3 electropolishing equipment and a 25 pct nitric acid + 75 pct methanol electrolyte at 30 V and −30 °C. The X-ray diffraction was carried out with a Rigaku X-ray diffractometer equipped with the JADE analyzing software and the JCPD database at a scan speed of 0.2 deg per minute, a step size of 0.01 deg, and a step holding time of 3 seconds. The microhardness was determined by using a Leitz Watzlar microhardness tester at a weight of 50 g.

Dumb-bell–shaped specimens with a 4-mm-diameter gage section and a gage length of 25 mm were used for both tensile and fatigue tests. The welded or HAZ simulated region was located at the center of the gage section. All specimens were polished by using 600-grit paper. Both tensile and fatigue tests were conducted with a computerized Instron 8502 servo-hydraulic testing system. Tensile properties were obtained at a strain rate of $1 \times 10^{-4}\ s^{-1}$ following the ASTM-E8M standard, and the fatigue life/strength was determined at room temperature, 50 Hz, and $R = 0.05$ or -1. The fatigue/endurance limit was defined as the cyclic stress level corresponding to 10^7 cycles without failure. Fracture surfaces of the tested specimens were examined by an SEM.

*JEOL is a trademark of Japan Electron Optics Ltd., Tokyo.

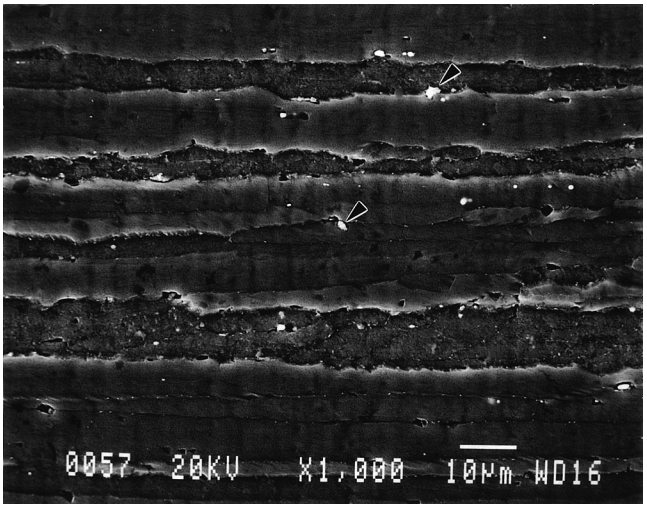

(*a*)

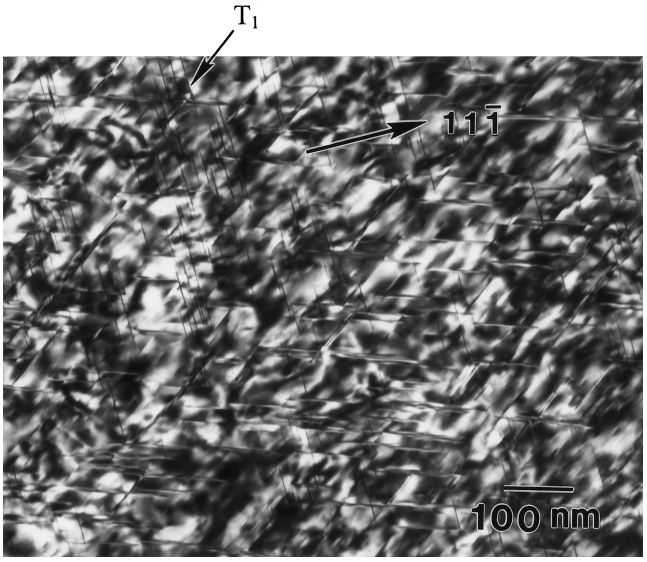

(*b*)

Fig. 2—Microstructures of the 2195-T8 base alloy: (*a*) SEM micrograph, and (*b*) TEM micrograph.

III. EXPERIMENTAL RESULTS

A. *Microstructures*

As reported in an earlier communication, the as-received material in the T8 temper (base alloy) consisted of pancake-shaped grains with a thickness of ~10 μm and a diameter of ~100 μm.[24] The elongated nature of grains in the as-received material is also shown in the SEM micrograph given in Figure 2(a). The occasionally observed undissolved

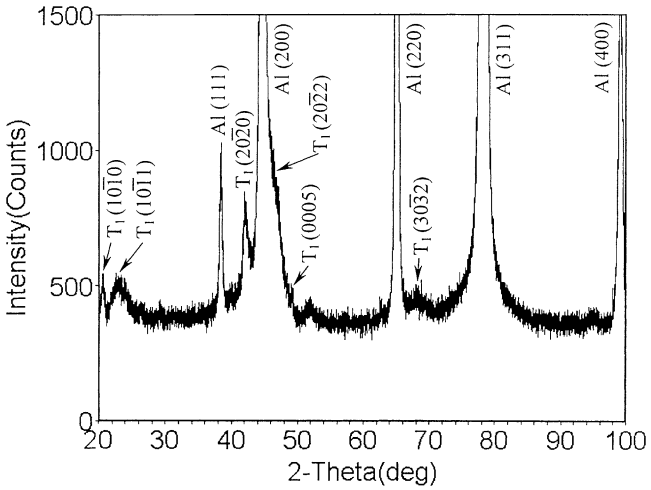

Fig. 3—X-ray diffraction pattern of the 2195-T8 base alloy.

particles/inclusions, indicated by arrows in the figure, were found by energy-dispersive spectroscopy and X-ray mapping to be Cu- and Fe-containing particles, as also reported earlier.[24] The TEM examination revealed that the main strengthening precipitates in the 2195-T8 alloy were predominantly T_1 phase, with platelet shapes aligned on {111} matrix planes, as shown in Figure 2(b). The identity of these precipitates was also confirmed by X-ray diffraction, as shown in Figure 3, where $(10\bar{1}0)$, $(10\bar{1}1)$, $(20\bar{2}0)$, and $(30\bar{3}2)$ T_1 peaks, without overlapping with any other peaks, were observed. The OIM measurements indicated that a brass-type texture, $\{110\}\langle 112\rangle$, was the predominant component, as also reported earlier.[24]

Figure 4 shows the SEM images of the specimens subjected to HAZ simulation at 400 °C, 550 °C, and 600 °C, respectively. It is seen that the HAZ simulation resulted in a pronounced change in the microstructure of the base alloy in the T8 temper. A number of precipitates formed mainly along the grain boundaries (GBs). The precipitates at the GBs increased and they became elongated with an increase in the simulation temperature. At 600 °C, microcracks and voids appeared at the GBs, and grains became larger and irregular, as shown in Figure 4(c). The X-ray diffraction studies revealed that the GB precipitates were T_B (Al_7Cu_4Li) phase, as shown in Figure 5. Obviously, after the HAZ simulation, the primary strengthening phase (T_1) in the T8 alloy disappeared, since no T_1 peaks were observed. The results of X-ray diffraction studies were also confirmed by TEM examinations. A representative micrograph of the specimen simulated at 600 °C is shown in Figure 6(a), which is the dark-field image obtained with a ~{111} matrix reflection. The typical coherency-strain-field contrast associated with δ' (Al_3Li) precipitates is visible. In addition, Guinier–Preston (G–P) zones were also observed. The presence of both δ' and G–P zones may be seen from the selected-area diffraction pattern taken in the $\langle 001\rangle$ beam direction, shown in Figure 6(b). Superlattice spots from the δ' precipitates are observed (indicated by arrows), and the streaks in the $\langle 001\rangle$ directions arise from the G–P zones. Qualitatively, with increasing HAZ simulation temperature, the number of δ' particles and G–P zones was observed to increase. The TEM observations also revealed that after the HAZ

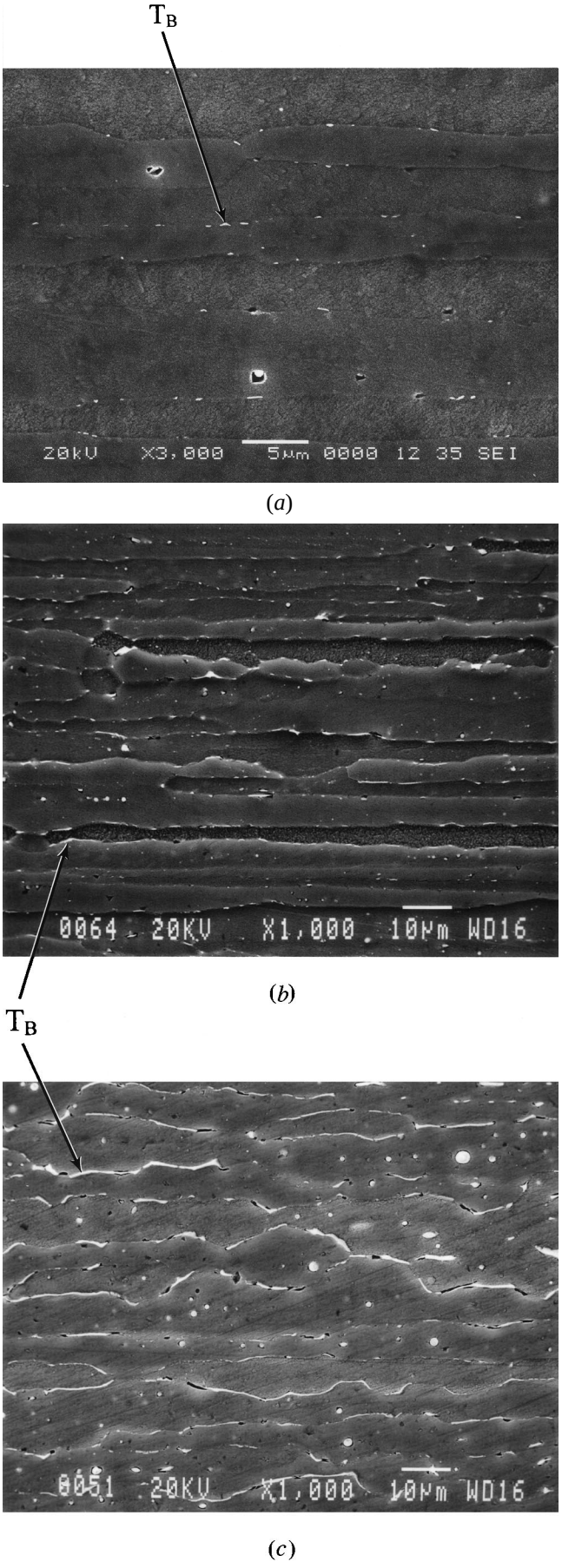

Fig. 4—SEM micrographs of the 2195 alloy after HAZ simulation: (*a*) 400 °C simulation, (*b*) 550 °C simulation, and (*c*) 600 °C simulation.

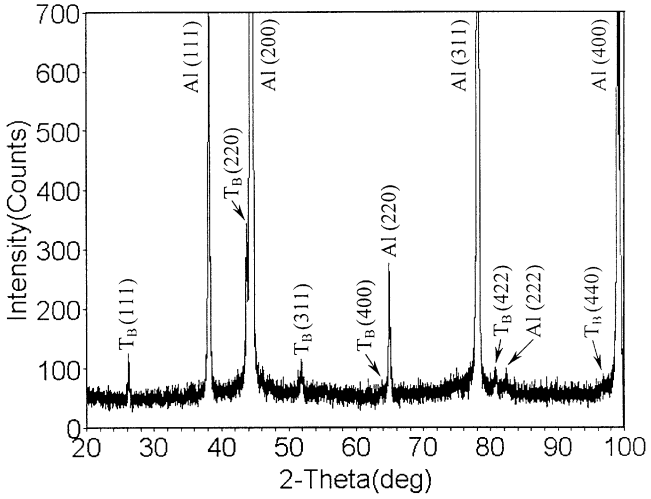

Fig. 5—X-ray diffraction pattern of the 2195 alloy after 600 °C simulation.

simulation, the T_1 primary strengthening phase totally disappeared.

Figure 7 shows the profile of the joint welded with 4043 filler alloy. Four passes of the weld can be identified, and some pores are also observed in both the FZ and HAZ, two of which are marked by arrows. A detailed examination by an SEM revealed that the precipitates were present mainly along the GBs in the HAZ close to the FZ, and example of which is shown in Figure 8(a). By X-ray diffraction, these precipitates were identified to be T_B phase. In the HAZ, microcracking or microfissuring was also observed on GBs close to the FZ, as shown in Figure 8(b).

As seen in Figure 8, numerous black particles and some white particles were embedded in the FZ. The black phase was analyzed and found to contain Al and Si, as shown by the EDS spectrum in Figure 9(a). It might also contain Li, which is unable to be detected by the EDS. The X-ray diffraction pattern obtained from the as-welded specimen (hereafter termed the W specimen), as shown in Figure 10, exhibited peaks due to the *T* (AlLiSi) compound, which has a cubic crystal structure, F-43m, and a lattice parameter of 0.593 nm.[25] Therefore, the black particles in the FZ are suggested to be *T* phase. The white phase in the FZ was observed to contain Al, Si, Fe, and Cu, as shown in Figure 9(b). It might also contain Li. The X-ray diffraction pattern did not show peaks due to a compound containing these elements, and its identity could not be established exactly. However, it could be Fe- and Cu-containing particles present as an impurity which was also present in the *T*8 alloy.[24] The volume fraction, number of particles per square millimeter, mean area, mean diameter, and aspect ratio of the *T* phase in the FZ are given in Table I for the as-welded material without a postweld heat treatment. It is seen that the volume fraction of the *T* phase was 4.6 pct, the number of particles per millimeter squared was 7910, and the aspect ratio was 1.8. The X-ray diffraction pattern in Figure 10 also exhibited a few Si peaks that might have been present as an impurity in the filler alloy. In addition, the T_1 phase was not observed in the HAZ adjacent to the FZ in the W material.

Figure 11 shows a typical micrograph taken close to the FZ interface in the welded specimen after having been postweld heat treated (hereafter termed the PWHT material).

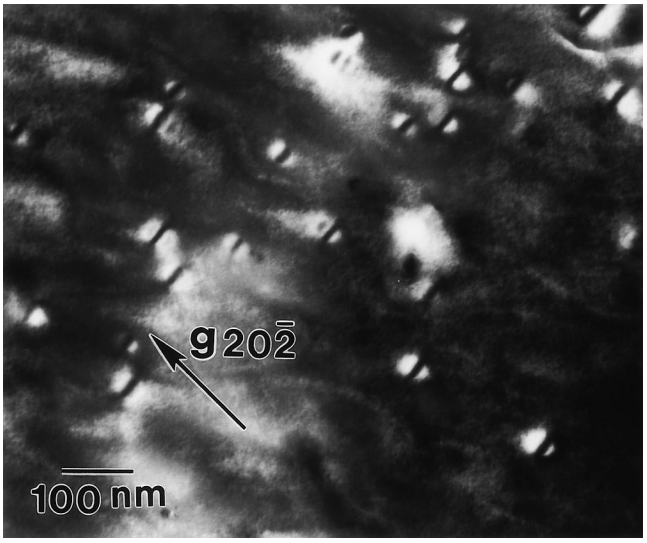

(*a*)

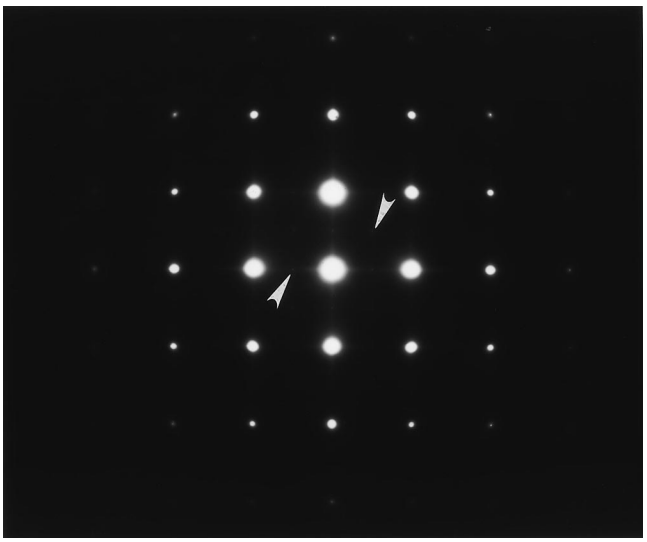

(*b*)

Fig. 6—(*a*) TEM micrograph (dark field) of the 2195 alloy after 600 °C simulation, and (*b*) its selected area diffraction pattern in ⟨001⟩ beam direction.

Apparently, both microcracks and *T* particles remained, and the microcracks became wider. The particles seen in the cracks are the mechanical polishing compound. Figure 12 demonstrates the microstructure in the FZ in the W specimen (Figure 12(a)) and the PWHT specimen (Figure 12(b)), respectively. The spheroidization of the primary *T* particles is seen to have occurred, and some small secondary *T* particles precipitated after the postweld heat treatment. The morphology and distribution of these particles were quantitatively analyzed by using Clemex image-analysis software. Table I lists the variation of various parameters of *T* particles in the FZ in both the W and PWHT materials. It is seen that after the postweld heat treatment, although the mean area and diameter remained almost unchanged, the volume fraction and number of *T* particles increased and the aspect ratio decreased. The X-ray diffraction analysis of the PWHT

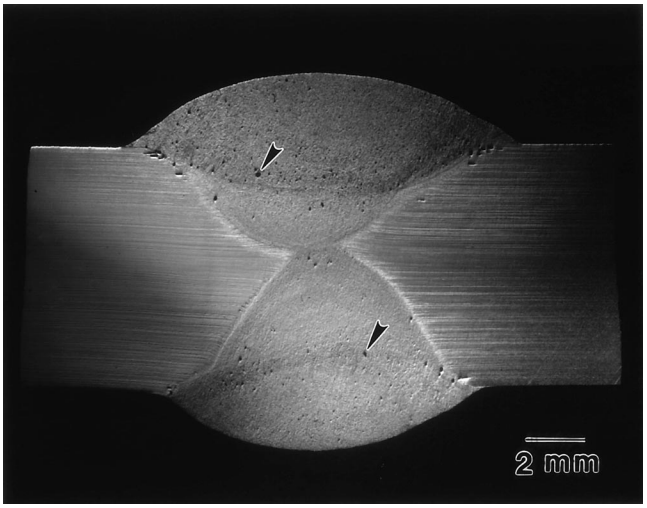

Fig. 7—Macroscopic profile of the 2195 welded joint, made with a 4043 filler metal.

specimen (Figure 13) confirmed that the postweld heat treatment resulted in the dissolution of T_B phase and a reappearance of T_1 phase in the HAZ. However, the T phase in the FZ was still present.

B. *Mechanical Properties*

1. *Hardness*

The microhardness of the T8 base alloy was determined to be about HV 185. A change in microhardness with distance from the center point of the specimen, where the thermocouple was spotwelded, is shown in Figure 14 for different HAZ simulation temperatures. The HAZ was limited to about 15 mm from the center point of the specimen. The rapid increase in hardness at a distance of about 16 to 18 mm is attributed to the reduction in temperature due to the cooling effects of the copper grips. As seen in this figure, the hardness is notably lower in the HAZ-simulated specimens than in the T8 base material. The minimum value of hardness, observed to occur at the center point of the specimens, decreased with an increase in the HAZ simulation temperature, *i.e.*, HV 140, HV 120, and HV 85 at 400 °C, 550 °C, and 600 °C, respectively. The hardness profile across the GTA weld is shown in Figure 15. It is seen that in the W material, the hardness was about HV 80 in the FZ and about HV 90 at the fusion boundary, similar to that obtained in the specimen that was HAZ simulated at 600 °C. However, the hardness of the HAZ in the W material was about HV 115, which is basically lower than that in the simulated HAZ, except for the region close to the center point. The postweld heat treatment resulted in an overall increase in the hardness in both the FZ and HAZ. The hardness value increased from about HV 80 to HV 130 in the FZ and from about HV 115 to HV 185 in the HAZ. That is, the hardness in the HAZ became the same as that of the base alloy.

2. *Tensile properties*

The tensile properties of the 2195-T8 alloy and those of the W and PWHT materials, in the longitudinal direction, are listed in Table II. It is seen that the tensile properties decreased significantly after welding. The yield strength was

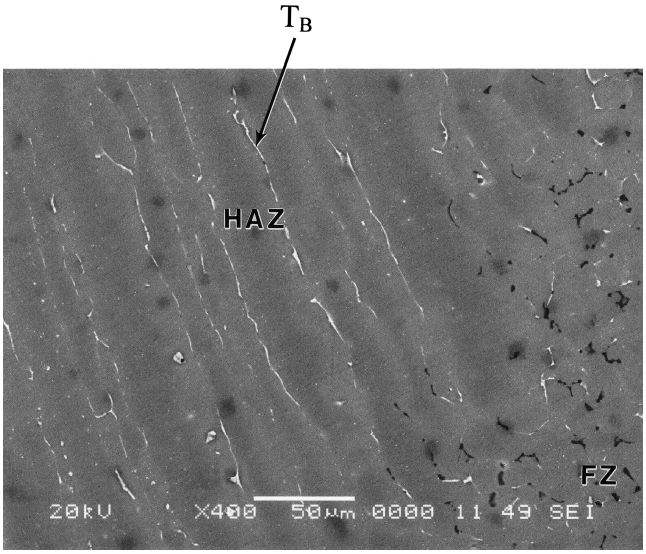

(*a*)

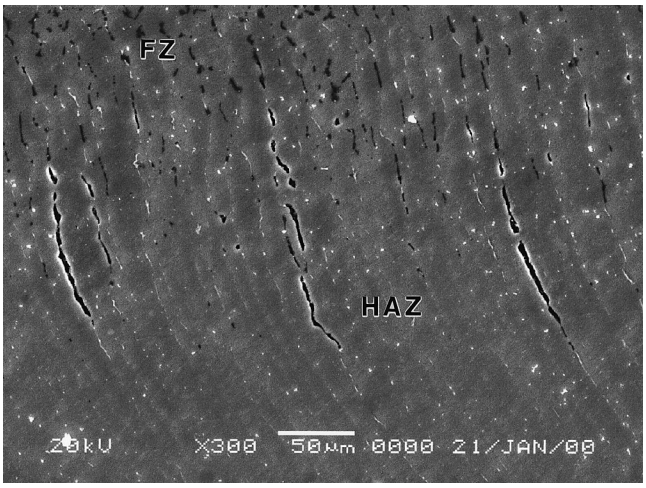

(*b*)

Fig. 8—Micrographs of the HAZ adjacent to the FZ boundary for the as-welded (W) specimen, showing (*a*) T_B phase along the GBs in the HAZ and (*b*) microcracks along the GBs in the HAZ.

about 41 pct of that of the T8 alloy, and the ductility was reduced to 2.1 pct from 12.8 pct. The postweld heat treatment resulted in a moderate increase in the yield strength and ultimate tensile strength, although the ductility decreased slightly. For instance, the yield strength increased from 41 to 59 pct of that of the base alloy.

The tensile properties as a function of HAZ simulation temperature are shown in Figure 16. It is seen that the HAZ simulation also caused a decrease in both the yield and ultimate tensile strengths. However, an increase in the simulation temperature from 400 °C to 580 °C resulted in a moderate increase in both the yield strength and ultimate tensile strength, but a significant decrease occurred when the simulation temperature exceeded 580 °C.

3. *Fatigue strength*

The plots of stress amplitude *vs* the number of cycles to failure, or S–N curves, for the 2195-T8 base alloy, HAZ-simulated material, and W and PWHT materials are shown

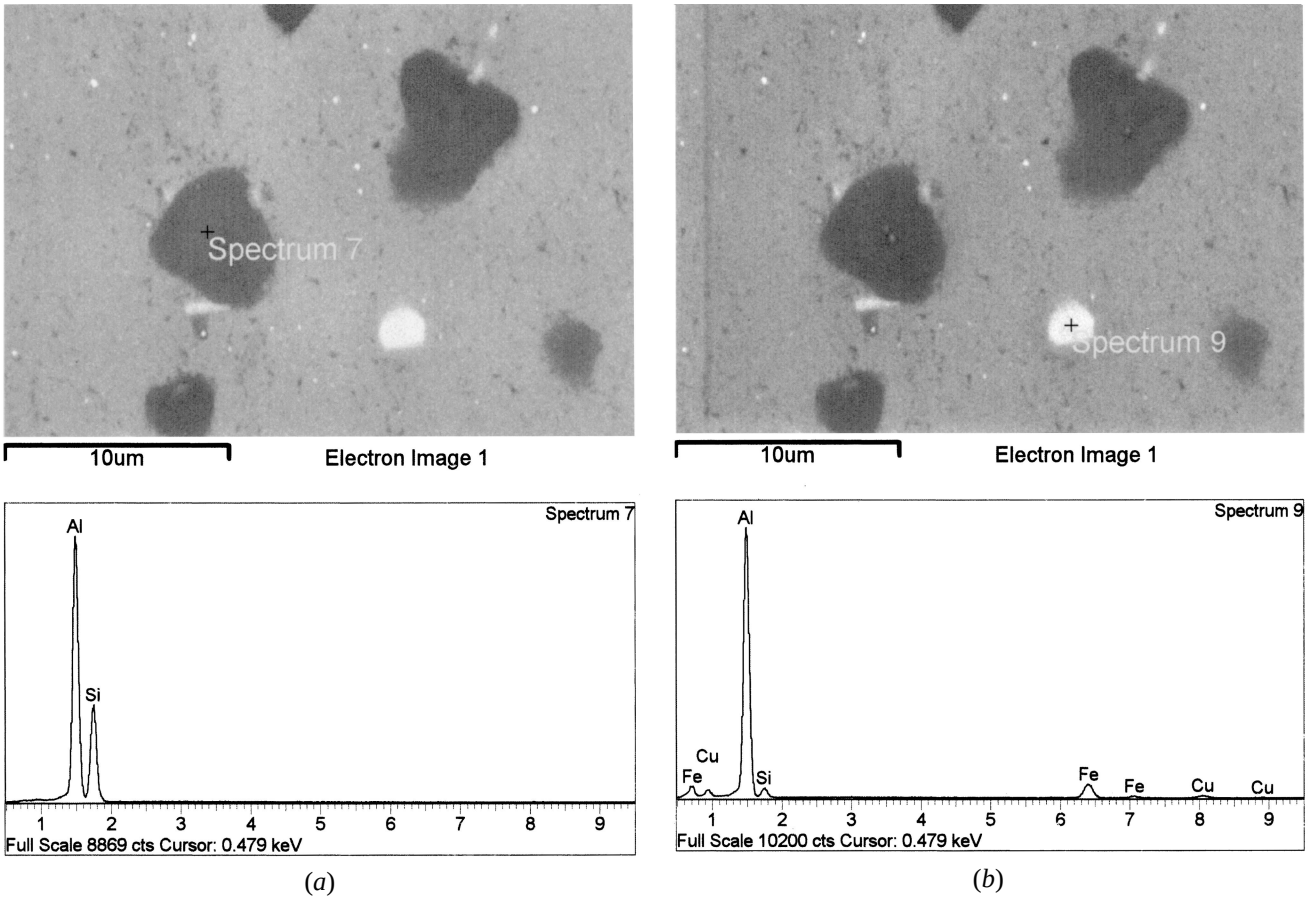

(*a*) (*b*)

Fig. 9—EDS spectrum of the 2195 alloy after welding with a 4043 filler metal. (*a*) Black phase in the FZ and (*b*) white phase in the FZ.

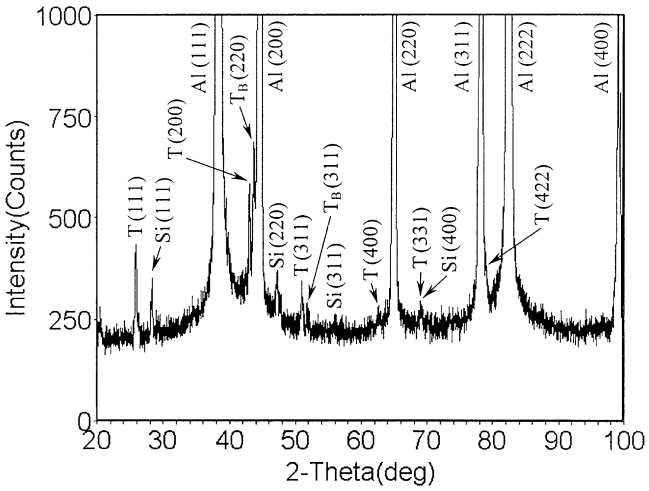

Fig. 10—X-ray diffraction spectrum of the 2195 alloy after welding with a 4043 filler metal.

Table I. Parameters Representing the Morphology and Distribution of T Particles in the FZ, Determined by the CLEMEX Image Analysis System, in the W and PWHT Materials

Parameters	W Material	PWHT Material
Volume fraction, pct	4.6	5.1
Number of particles per mm^2	7910	8617
Mean area, μm^2	5.8	5.9
Mean diameter, μm	2.4	2.5
Mean aspect ratio	1.80	1.56

Notes: W material—as-welded joint without postweld heat treatment, PWHT material—welded joint after postweld heat treatment.

in Figure 17. The HAZ simulation was observed to have a considerable influence on the fatigue strength. The fatigue strength decreased drastically with an increase in the simulation temperature. The fatigue limit of the alloy after the HAZ simulation at 550 °C and 600 °C was approximately 83 and 57 pct of that of the T8 base alloy. The fatigue limit of the W and PWHT materials was even lower, being almost 28 pct of that of the T8 alloy. As shown in Figure 17, the fatigue strength did not improve by the postweld heat treatment, although the yield and ultimate tensile strengths increased by about 42 and 15 pct, respectively (Table II).

C. *Fractography*

1. *Tensile fracture surfaces*

It was observed that in tensile tests, almost all the specimens of the T8 base alloy and HAZ-simulated material fractured at a “slant” or in a quasi-shear mode. A similar fracture mode was also observed by Venkateswara Rao and Ritchie in a 2090-T83 alloy tested at room temperature.[26] Detailed SEM observations of the tensile fracture surfaces

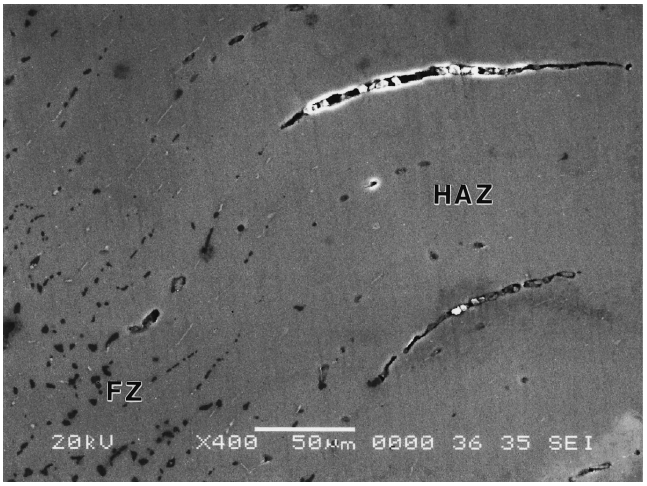

Fig. 11—HAZ adjacent to the FZ boundary after welding with a 4043 filler metal and postweld heat treatment (SEM micrograph).

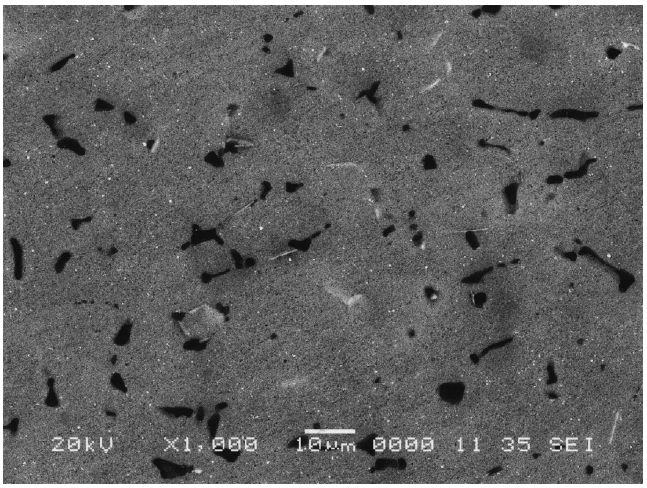

(*a*)

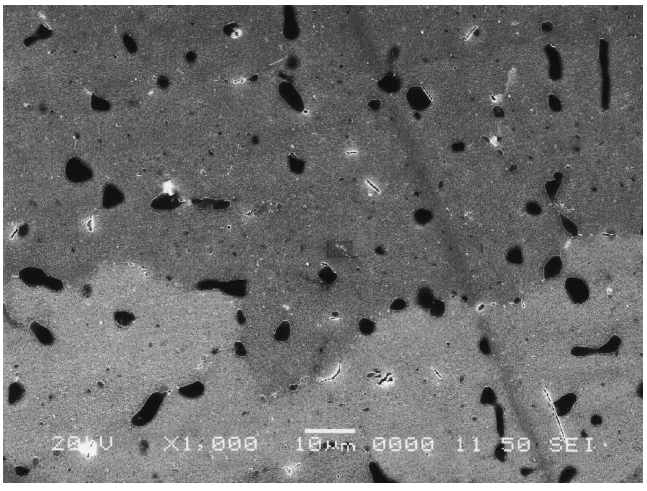

(*b*)

Fig. 12—Microstructures of the FZ in (*a*) W material and (*b*) PWHT material.

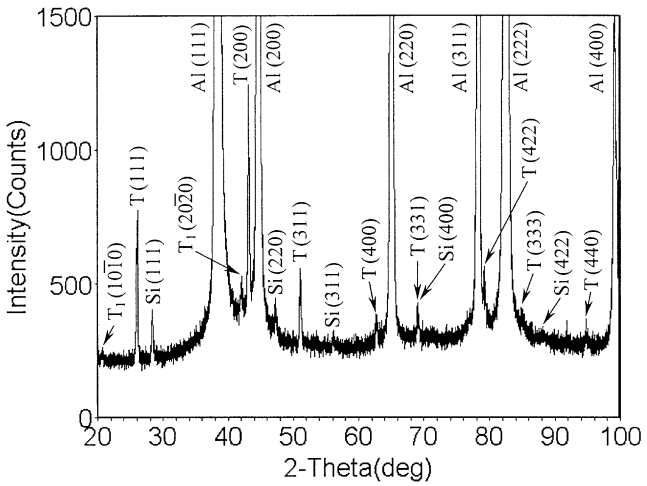

Fig. 13—X-ray diffraction spectrum of the PWHT material.

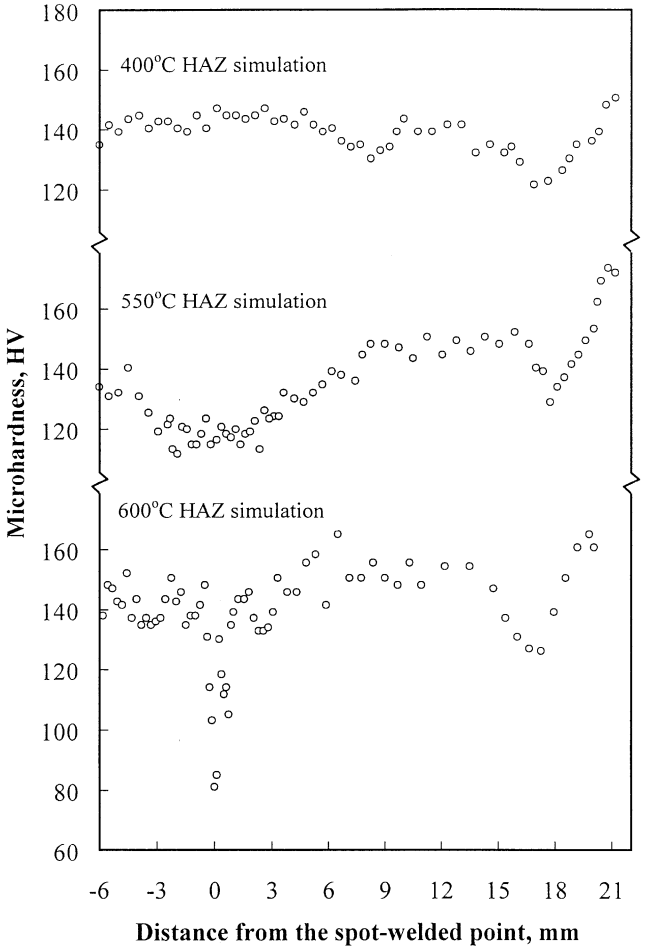

Fig. 14—Microhardness profile of the 2195 alloy after HAZ simulation at 400 °C, 550 °C, and 600 °C.

of the T8 alloy and HAZ-simulated material are shown in Figures 18(a) and (b). The tensile fracture surface of the T8 alloy clearly exhibits shear steps perpendicular to the shear direction, with the step height (Figure 18(a)) being almost equivalent to the thickness of the pancake-shaped grains in the material (Figure 2(a)). In spite of the similar macroscopic fracture mode in the T8 base alloy and in the HAZ-simulated material, the microscopic morphology of the fracture surface

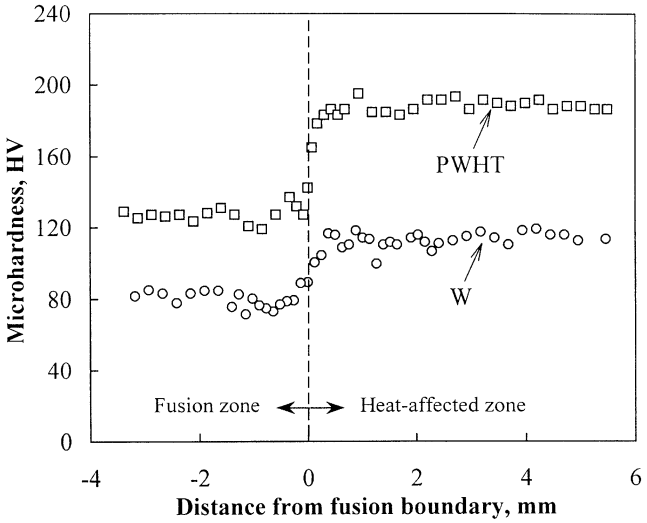

Fig. 15—Microhardness profile of the W and PWHT materials.

Table II. Tensile Properties of the 2195 Al-Li Alloy in Different States

Material States	Yield Strength, MPa	Ultimate Tensile Strength, MPa	Elongation, Pct
T8 base alloy	549	585	12.8
W material	227	302	2.1
PWHT material	322	347	1.5

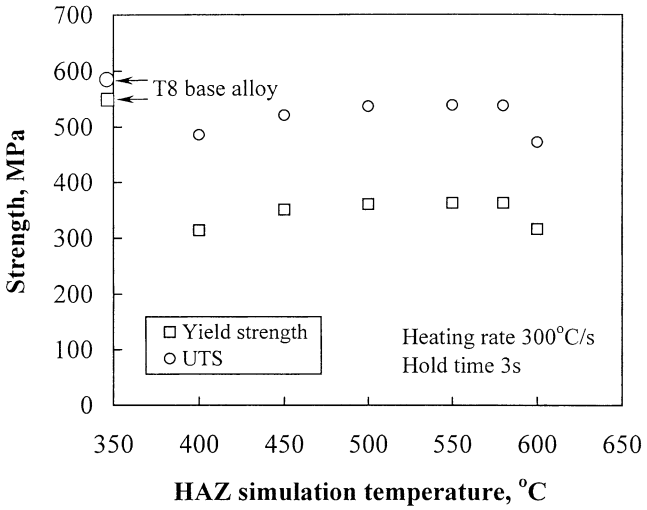

Fig. 16—Yield strength and ultimate tensile strength as a function of HAZ simulation temperature at a heating rate of 300 °C/s and holding time of 3 s.

of the two materials was observed to be different. No regular shear steps were observed in the HAZ-simulated material, as shown in Figure 18(b).

Figure 19 demonstrates the tensile fracture surfaces of the W and PWHT materials. It is seen that cleavage cracking was predominant in the W material (Figure 19(a)), while cleavage cracking coupled with an intergranular microvoid coalescence fracture mechanism occurred in the PWHT material (Figure 19(b)). It should be noted that in the W

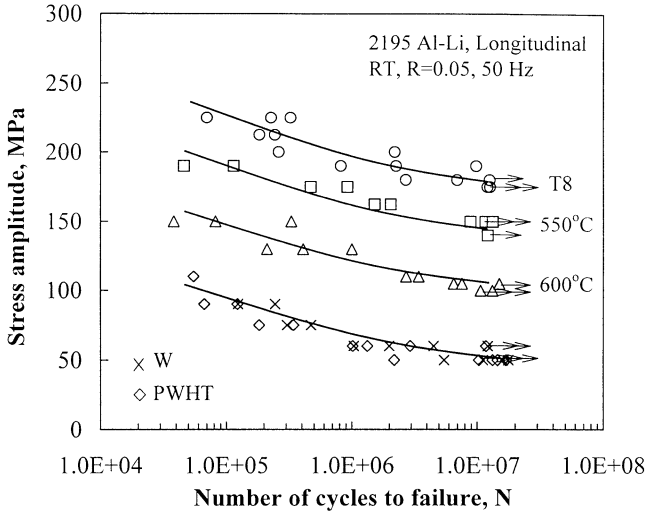

Fig. 17—Influence of HAZ simulation (at 550 °C and 600 °C) and welding with a 4043 filler metal (with and without postweld heat treatment) on S–N curves of the specimens tested at RT, 50 Hz, and $R = 0.05$.

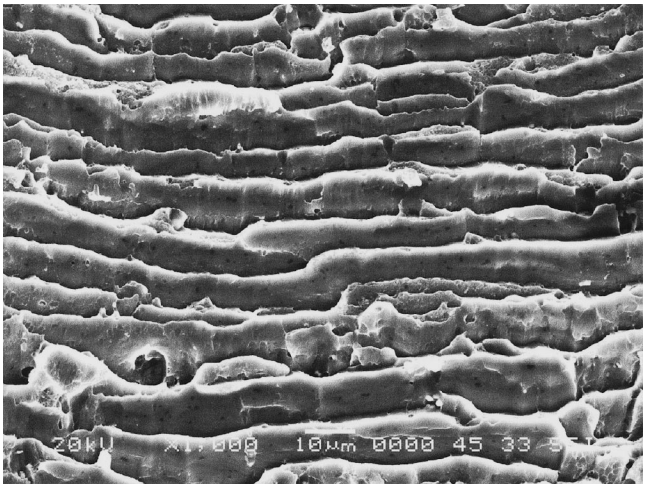

(*a*)

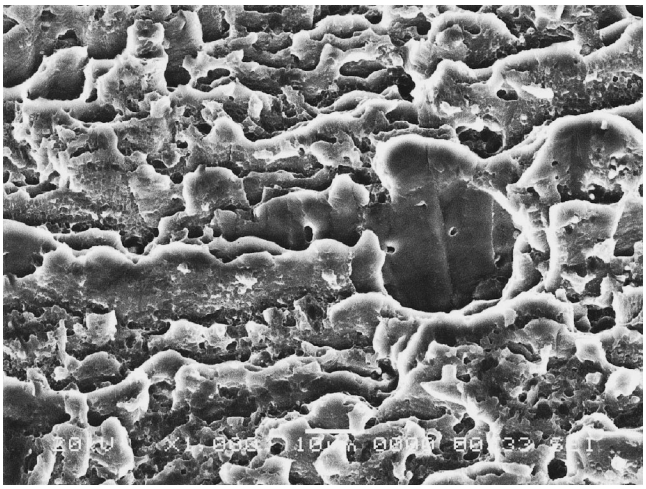

(*b*)

Fig. 18—SEM micrographs illustrating the tensile fracture surfaces of the 2195 alloy. (*a*) T8 base alloy and (*b*) 600 °C HAZ simulation.

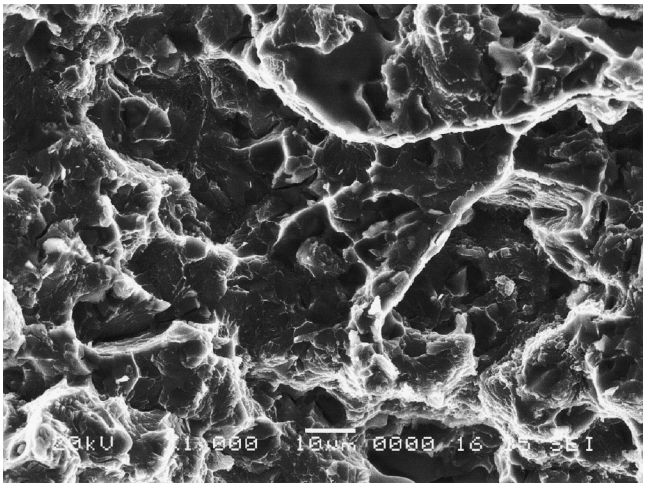

(*a*)

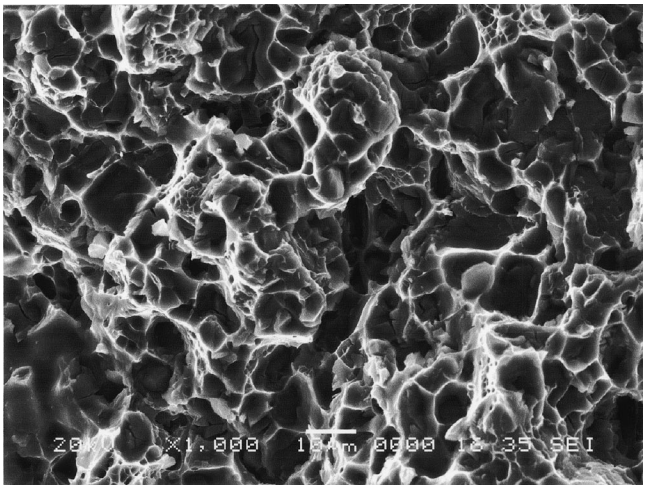

(*b*)

Fig. 19—SEM micrographs illustrating the tensile fracture surfaces of the 2195 weld joint: (*a*) W material and (*b*) PWHT material.

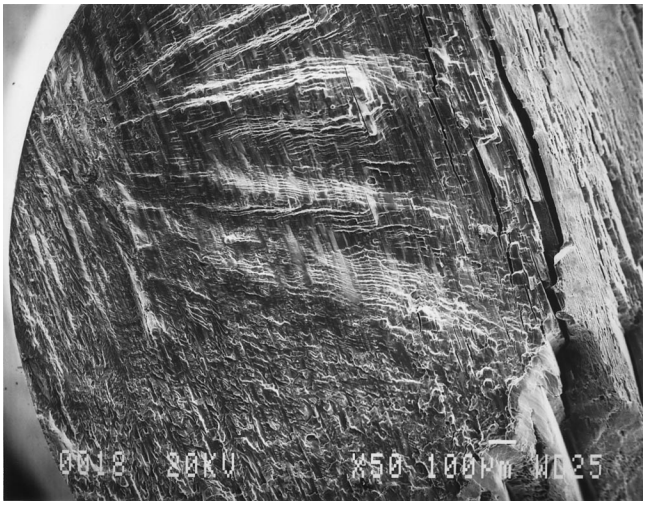

(*a*)

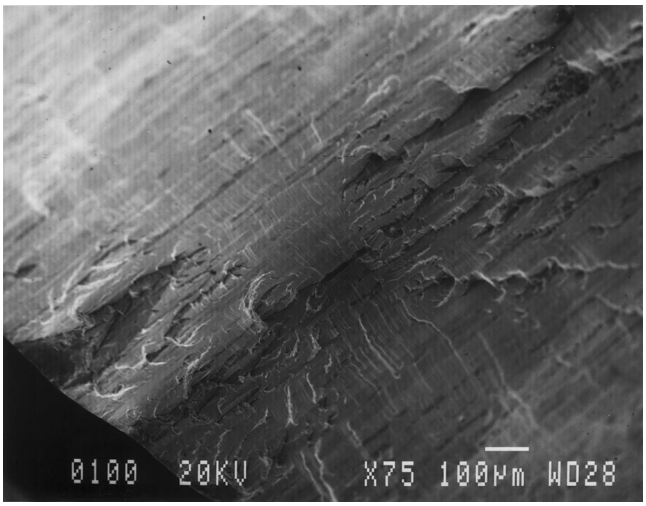

(*b*)

Fig. 20—Low-magnification SEM micrographs of fatigue fracture surfaces of the 2195 alloy tested at RT, 50 Hz, and $R = 0.05$: (*a*) T8 base alloy and (*b*) 600 °C HAZ simulation.

material, the macroscopic shear fracture was not observed, with the fracture surfaces being perpendicular to the tensile axis. The tensile fracture occurred in the FZ, irrespective of the postweld heat treatment.

2. *Fatigue fracture surfaces*

The low-magnification SEM fractographs of fatigue fracture of the T8 base alloy and HAZ-simulated material are shown in Figures 20(a) and (b), respectively. It is seen that in the T8 alloy, the fatigue cracks initiated generally from the specimen surfaces. However, the initiation of the fatigue cracks after the HAZ simulation occurred basically at the interior defects in the specimens (Figure 20(b)). Figure 21 shows the fractography of the crack-growth area at higher magnifications. It is seen that fatigue striation was a typical feature of the fatigue fracture in the T8 base alloy, as shown in Figure 21(a). The striation spacings increased with increasing distance from the initiation site, indicating that the crack growth rate increased gradually with increasing crack length. In the HAZ-simulated specimens, the fatigue fracture surface was basically characterized by cleavage-like cracking and an absence of fatigue striations (Figure 21(b)).

Although all the tensile specimens fractured in the FZ, unaided visual examination of the fracture location suggested that the fatigue fracture occurred in either the FZ or the HAZ, with almost the same probability, in the W material. However, in the PWHT specimens, the fatigue fracture occurred mainly in the HAZ. A typical example of the fatigue fracture surface in the HAZ in the PWHT material is shown in Figures 22(a) and (b). The low-magnification micrograph (Figure 22(a)) shows that the fatigue crack originated at a defect in the HAZ. At higher magnification the fracture surface was observed to exhibit cleavage fracture characteristics, as shown in Figure 22(b).

IV. DISCUSSION

A. *Effect of HAZ Simulation and Welding on Microstructures*

The major strengthening phase in the 2195-T8 base alloy was observed to be the homogeneously distributed fine T_1 precipitates, although other phases, such as θ' (Al_2Cu), S' (Al_2CuMg) δ' (Al_3Li), and β' (Al_3Zr) have been also

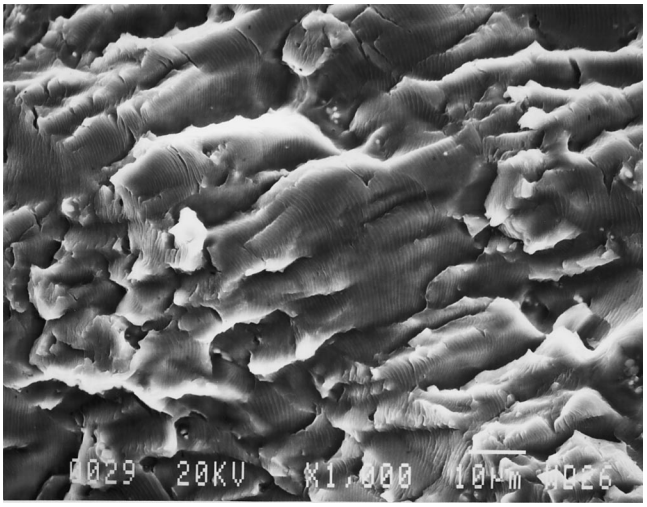

(*a*)

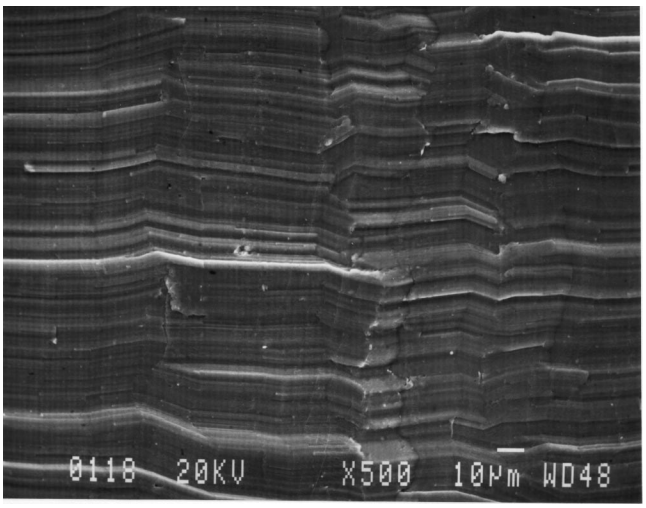

(*b*)

Fig. 21—Higher-magnification SEM micrographs of fatigue fracture surfaces of the 2195 alloy tested at RT, 50 Hz, and $R = 0.05$: (*a*) T8 base alloy and (*b*) 600 °C HAZ simulation.

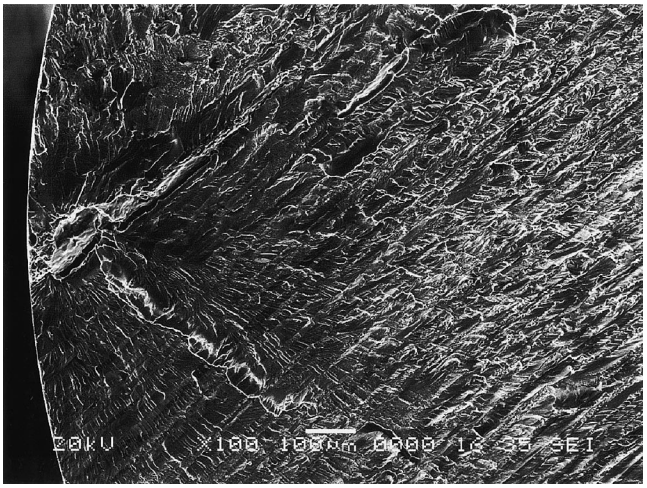

(*a*)

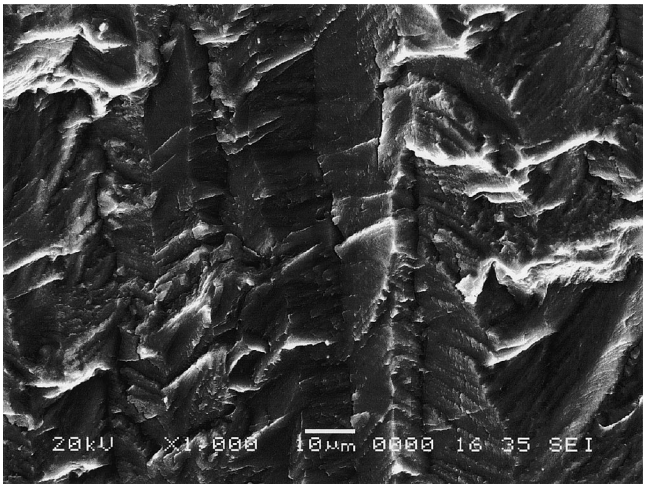

(*b*)

Fig. 22—SEM micrographs of fatigue fracture surfaces of the PWHT material: (*a*) low-magnification micrograph showing a full view of the fracture surface and (*b*) higher-magnification micrograph showing the crack propagation area.

reported in the literature.[1,3,5,8,27] It was observed that the HAZ simulation caused dissolution of T_1 phase, as shown in Figures 4 through 6. This is in agreement with the reported effect of friction stir welding[18] and variable-polarity plasma arc welding.[20] In the latter research, the dissolution was observed to occur at 320 °C. This is consistent with the results of the present study, where the HAZ simulation temperatures were between 400 °C and 600 °C. The HAZ simulation also involved quasi-quenching (a compressed helium quench), followed by storing the specimens at room temperature for a few days before TEM examination and mechanical testing. Therefore, the HAZ-simulated material went through a natural aging process which would produce G–P zones and δ' phase, as natural aging is known to occur in this way in the AA2095 and 2195 Al-Li alloys.[8,28,29] The formation of dislocations after HAZ simulation is probably caused by the residual internal stresses produced during thermal cycling.[30] A higher HAZ simulation temperature would increase the degree of supersaturation of solute atoms due to the increased dissolution of T_1 phase, giving rise to the observed increase in the amount of G–P zones and δ' precipitates. The increased supersaturation would also explain the formation of T_B phase in the material that was subjected to the HAZ simulation at higher temperatures. These microstructural changes resulted in a slight increase in the tensile strength with increasing simulation temperatures up to 580 °C for the HAZ-simulated material, as shown in Figure 16. The reduction of the tensile strength for the 600 °C HAZ simulation is attributed to microcracks and voids (Figure 4(c)) formed due to the contraction stresses during the cooling phase of the simulation. The presence of these defects is also the cause for the observed sharp decrease in the hardness (Figure 14(c)) when the HAZ simulation was conducted at 600 °C.

The FZ in the W material consisted of a typical composite-type structure, with *T* particles embedded in the matrix, as shown in Figure 12. The 4043 alloy selected as the filler metal does not contain the alloying element Li. The Li in the observed *T* phase can, therefore, only be derived from the melted base alloy during welding. Since the diffusion of Li in Al is very rapid,[25,31] the *T* particles were observed

to form uniformly throughout the entire fusion zone (Figure 12). A noteworthy microstructural feature in the W specimens was the occurrence of microcracking and T_B phase along the GBs in the HAZ in the vicinity of the fusion boundary (Figure 8), which was also observed in the HAZ-simulated specimens at 600 °C (Figure 4(c)). During welding, the high peak temperatures experienced immediately adjacent to the fusion boundary caused a complete dissolution of T_1 precipitates and the formation of liquated phases.[17] It is suggested that the microcracking is closely related to the liquation, and the formation of T_B phase is associated with the diffusion of solute elements at high temperatures. Both the HAZ simulation and actual welding resulted in similar microstructural characteristics in the HAZ, *i.e.*, the formation of T_B phase and microcracks. The consumption of solute elements by the formation of T_B phase in the HAZ close to the fusion boundary, and especially by the formation of *T* phase in the FZ, would result in a reduction in solid-solution hardening. Consequently, a drastic hardness change in the HAZ at a distance of about 0.5 mm from the fusion boundary was observed, as shown in Figure 15.

The postweld heat treatment modified the microstructure of the weld. It can be seen from Figure 12 that the *T* particles were more irregular in the W material and more spherical in the PWHT material. In particular, some small secondary *T* particles, which precipitated during the postweld heat treatment, can be identified among the primary *T* particles, which formed during solidification of the 4043 filler alloy. The precipitation of these small particles, the mechanism of which needs to be studied further, gave rise to an increase in the number of *T* particles and a smaller average interparticle spacing Figure 12(b). The results of quantitative metallography, given in Table I, clearly indicate an increase in the volume fraction and the number of *T* particles per unit area and a decrease in the aspect ratio in the PWHT material. As a result, both the hardness of the FZ (Figure 15) and the overall strength (Table II) increased after the postweld heat treatment. The increase in hardness in the HAZ (Figure 15) is attributed to the dissolution of T_B phase during solution treatment and the reprecipitation of the T_1 primary strengthening phase after the subsequent artificial aging treatment, as illustrated in Figures 10 and 13. Although the hardness in both the FZ and HAZ increased after the postweld heat treatment, the microcracks in the HAZ close to the FZ interface did not disappear. On the contrary, they appeared to open wider (Figure 11). Therefore, no increase in the fatigue strength was observed after the postweld heat treatment, as shown in Figure 17.

B. *Effect of HAZ Simulation and Welding on Tensile Properties*

As shown in Figure 16, as the HAZ simulation temperature increased, both the yield and ultimate tensile strengths first increased and then decreased, reaching a peak at about 550 °C to 580 °C. Martukanitz *et al.*[30] have also observed that the microhardness across the HAZ of the variable-polarity plasma arc welds in the 2195-T8 alloy had a minimum value at a distance of about 7 mm from the fusion boundary, and then it increased and reached a value close to the hardness of the base material at a distance of approximately 25 to 30 mm from the fusion boundary.[20,30] The hardness profile

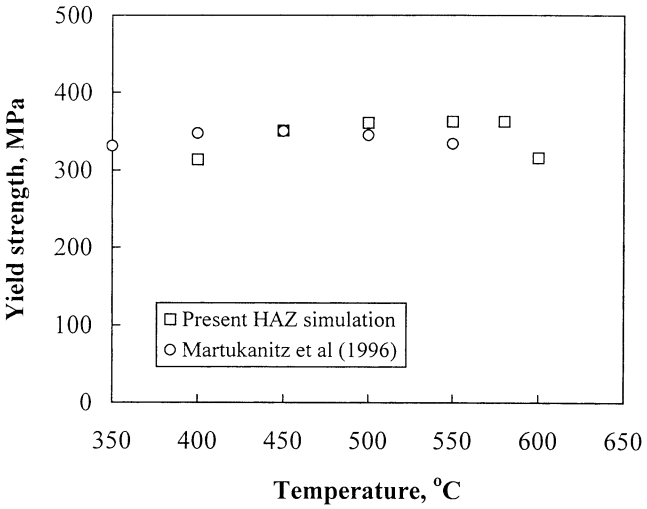

Fig. 23—A comparison between the yield strength of the HAZ-simulated specimens and that converted from the hardness profile across the HAZ. [30]

reported by Martukanitz *et al.*[30] was converted to yield strength based on the following relationship, suggested by Cahoon *et al.*[32]:

$$\sigma_{0.2} = 3.27HB^n \qquad [1]$$

where $\sigma_{0.2}$ is the 0.2 pct offset yield strength in mega Pascals, *H* is the Diamond pyramid hardness number, *n* is the strain-hardening exponent, and *B* is a constant which is equal to 0.1 for both aluminum and steel. The calculated values of yield strength across the HAZ are plotted in Figure 23. It is seen that the general profile of the variation in the calculated value of the yield strength across the HAZ, based on the hardness profile reported by Martukanitz *et al.*,[30] is very similar to the actual variation of the yield strengths with the HAZ simulation temperature. The variation in the yield and ultimate tensile strengths with the HAZ simulation temperature is attributed to the change in microstructures, as discussed earlier.

A significant reduction in yield strength of the W material (Table II) is suggested to be directly associated with the microstructure of the 4043 filler alloy, because the tensile fracture invariably occurred in the FZ (Figure 19), in spite of the presence of microcracks in the HAZ. As discussed earlier, the increase in the yield strength of the PWHT material is mainly attributed to the modification of the microstructure in the FZ and the formation of small secondary *T* particles. The increased number of *T* particles gave rise to a smaller interparticle spacing, resulting in an increase in the yield strength of the FZ and, thus, the PWHT material.

C. *Effect of HAZ Simulation and Welding on Fatigue Strength*

As shown in Figure 17, the 550 °C and 600 °C HAZ simulation resulted in a significant decrease in the fatigue strength/limit, compared with the 2195-T8 alloy. This could be due to the fact that the fatigue limit of a material is generally higher when its tensile strength is larger.[33] Since the 550 °C simulation resulted in only a moderate reduction in the tensile strength, the fatigue strength of the material was reduced by only about 17 pct of the T8 alloy. Furthermore, the tendency of T_B particles to resist fatigue crack

growth[34] may also have contributed to a relatively smaller reduction in the fatigue strength.

A significant decrease in the fatigue strength after the 600 °C simulation is attributed to a further reduction in the tensile strength (Figure 16), the network-like distribution of T_B phase, and, especially, the presence of microcracks/voids along the GBs (Figure 4(c)), because the fatigue cracks can easily initiate from these sites (Figure 20(b)). Moreover, the coarsening of grains after the 600 °C simulation would have also reduced the fatigue limit, since its dependence on grain size has been found to obey Hall–Petch relationship.[35] Plumtree[36] has also predicted, through modeling, a decrease in the fatigue/endurance limit with an increase in the grain size. Therefore, based on the previous considerations, the fatigue limit of the HAZ-simulated material at 600 °C should be significantly reduced, as observed in Figure 17.

The SEM fractography (Figures 20 and 21) also indicated that, contrary to the base alloy, the crack initiation in the HAZ-simulated material occurred mainly at the interior defects, and the subsequent crack propagation was characterized by brittle cleavage-like fracture. Thus, the alloy after the HAZ simulation exhibited a lower fatigue strength. The pronounced reduction in fatigue strength after the 600 °C simulation is associated with both easier initiation and propagation of the fatigue crack, due to the presence of microcracks and voids.

The reason for the lower fatigue strength of the W material is related to the lower strength and ductility in the FZ and, especially, to microcracks in the HAZ. The location of fatigue-crack initiation is dependent on the relative weakness in both the FZ and HAZ. It seems that in the W material, the FZ and HAZ were almost equally weak, because the probability of fatigue fracture occurring in both zones was observed to be almost the same. Although the applied postweld heat treatment resulted in an increase in the strength in the FZ (Table II), the microcracks in the HAZ remained. In this situation, the HAZ could be weaker than the FZ. As a result, the majority of the fatigue fracture occurred in the HAZ (Figure 22), and there was no increase in the fatigue strength after the postweld heat treatment, as shown in Figure 17.

V. SUMMARY AND CONCLUSIONS

1. The microstructure of the 2195-T8 Al-Li alloy consisted of pancake-shaped grains. The primary strengthening precipitates of the alloy were of T_1 phase, with platelet shapes on {111} matrix planes. The texture of the alloy was predominantly of the brass type, $\{110\}\langle 112\rangle$.
2. The HAZ simulation resulted in the dissolution of T_1 phase and the formation of T_B phase along the GBs. The microstructure after the HAZ simulation consisted mainly of a mixture of G-P zones and δ' phase. When the simulation temperature increased from 550 °C to 600 °C, both the grain size and the amount of T_B phase increased, and microcracks and voids formed along the GBs.
3. After welding with a 4043 filler metal, T phase formed and was uniformly distributed in the FZ. An elongated T_B phase and microcracks were observed to occur along the GBs in the HAZ. No T_1 phase could be identified in the HAZ adjacent to the fusion boundary.
4. The postweld heat treatment resulted in the spheroidization of primary T phase and the precipitation of small secondary T particles. However, the microcracks remained and became wider than those observed in the as-welded condition. After the heat treatment, the T_B phase in the HAZ disappeared, which was replaced by the reprecipitation of T_1 phase.
5. Both the HAZ simulation and welding resulted in a considerable decrease in the fatigue strength, which was also accompanied by a significant reduction in the hardness and tensile properties. The hardness of the FZ was less than that of the HAZ. The postweld heat treatment resulted in an increase in both the hardness and tensile strength, due to the reprecipitation of T_1 phase in the HAZ and the smaller interparticle spacing in the FZ. However, the fatigue strength did not improve because of the presence of microcracks in the HAZ.
6. Fatigue-crack initiation generally occurred at the surface in the T8 base alloy and at the interior defects (microcracks and voids) in the HAZ-simulated and welded materials. Fatigue-crack propagation exhibited characteristic striations in the T8 alloy and brittle cleavage-like cracking in the HAZ-simulated and welded specimens.

ACKNOWLEDGMENTS

The financial support provided by a consortium of Manitoba aerospace industries and the Natural Sciences and Engineering Research Council (NSERC) of Canada is gratefully acknowledged. The authors thank Drs. N. Goel and N. Richards for arranging the welding of specimens at Bristol Aerospace Ltd. (Winnipeg, MB, Canada); H.W. Guo, W.J. Fan, Ms. U. Prasad, and Messrs. J. Van Dorp and D. Mardis for their assistance with experimental work; and Dr. S. Laroche, Clemex Technologies Inc. (Langueuil, Quebec, Canada), for doing the quantitative metallography.

REFERENCES

1. F.W. Gayle, W.T. Tack, G. Swanson, F.H. Heubaum, and J.R. Pickens: *Scripta Metall. Mater.*, 1994, vol. 30, pp. 761-66.
2. D. Furrer and R. Noel: *Adv. Mater. Processes*, 1997, vol. 151, pp. 59-60.
3. P.S. Chen, A.K. Kuruvilla, T.W. Malone, and W.P. Stanton: *J. Mater. Eng. Performance*, 1998, vol. 7, pp. 682-690.
4. S.J. Hales and R.A. Hafley: *Mater. Sci. Eng. A*, 1998, vol. A257, pp. 153-64.
5. B.P. Huang and Z.Q. Zheng: *Scripta Mater.*, 1998, vol. 38, pp. 357-62.
6. B.P. Huang, Z.Q. Zheng, D.F. Yin, and Z.M. Mo: *Mater. Sci. Forum*, 1996, vols. 217–222, pp. 1239-44.
7. R. Crooks, Z. Wang, V.I. Levit, and R.N. Shenoy: *Mater. Sci. Eng. A*, 1998, vol. A257, pp. 145-52.
8. K.S. Kumar, S.A. Brown, and J.R. Pickens: *Acta Mater.*, 1996, vol. 44, pp. 1899-1915.
9. P.N. Kalu and L. Zhang: *Scripta Mater.*, 1998, vol. 39, pp. 175-80.
10. J.C. Lippold and W. Lin: *Mater. Sci. Forum*, 1996, vols. 217–222, pp. 1685-90.
11. P. Chien: *Welding J.*, 1998, vol. 77, pp. 45-47.
12. R. Jan, P.R. Howell and R.P. Martukanitz: in *Trends in Welding Research*, H.B. Smartt, J.A. Johnson, and S.A. David, ASM INTERNATIONAL, Materials Park, OH, 1996, pp. 329-34.
13. D.K. Aidun and J.P. Dean: *Welding J.*, 1999, vol. 78, pp. 349s-354s.
14. A. Kostrivas and J.C. Lippold: *Welding J.*, 2000, vol. 79, pp. 1s-8s.
15. M.P. Nemeth, R.D. Young, R.J. Collins, and J.H. Starnes: *J. Spacecraft Rockets*, 1999, vol. 36, pp. 812-19.
16. L.E. Murr, Y. Li, E.A. Trillo, B.M. Nowak, and J.C. McClure: *Alum. Trans.*, 1999, vol. 1, pp. 141-54.

17. K.H. Hou and W.A. Baeslack III: *J. Mater. Sci. Lett.*, 1996, vol. 15, pp. 208–13 and pp. 239-44.
18. Z.X. Li, W.J. Arbegast, P.J. Hartley and E.I. Meletis: in *Trends in Welding Research*, J.M. Vitek, S.A. David, J.A. Johnson, H.B. Smartt, and T. DebRoy, ASM INTERNATIONAL, Materials Park, OH, 1999, pp. 568-73.
19. W.J. Arbegast, K.S. Baker, and P.J. Hartley: in *Trends in Welding Research*, J.M. Vitek, S.A. David, J.A. Johnson, H.B. Smartt, T. DebRoy, eds. ASM INTERNATIONAL, Materials Park, OH, 1999, pp. 558-62.
20. R.P. Martukanitz and P.R. Howell: in *Trends in Welding Research*, H.B. Smartt, J.A. Johnson, and S.A. David, ASM INTERNATIONAL, Materials Park, OH, 1996, pp. 553-62.
21. R.P. Martukanitz, A.L. Wilson, and P.R. Howell: *Mater. Sci. Forum*, 2000, vols. 331–337, pp. 1291-96.
22. K. Easterling: *Introduction to the Physical Metallurgy of Welding*, 2nd ed. Butterworth-Heinemann Ltd., Oxford, United Kingdom, 1992.
23. W. Hu and E.I. Meletis: *Mater. Sci. Forum*, 2000, vols. 331–337, pp. 1683-88.
24. D.L. Chen and M.C. Chaturvedi: *Mater. Metall. Trans.* A, 2000, vol. 31A, pp. 1531-41.
25. N.C. Goel and J.R. Cahoon: *J. Phase Equilibria*, 1991, vol. 12, pp. 225-30.
26. K.T. Venkateswara Rao and R.O. Ritchie: *Acta Metall Mater.*, 1990, vol. 38, pp. 2309-26.
27. B.P. Huang and Z.Q. Zheng: *Acta Mater.*, 1998, vol. 46, pp. 4381-93.
28. F.W. Gayle, F.H. Heubaum, and J.R. Pickens: *Scripta Metall. Mater.*, 1990, vol. 24, pp. 79-84.
29. C.P. Blankenship, Jr. and E.A. Starke, Jr.: *Fatigue Fract. Eng. Mater. Struct.*, 1991, vol. 14, pp. 103-14.
30. R.P. Martukanitz, P.R. Howell, E.A. Payzant, S. Spooner, and C.R. Hubbard: in *Nondestructive Evaluation and Materials Properties III*, P.K. Liaw, O. Buck, R.J. Arsenault, and R.E. Green, Jr., eds. TMS-AIME, 1996, pp. 89-95.
31. V. Burachynsky and J.R. Cahoon: *Metall. Mater. Trans.*, *A*1997, vol. 28A, pp. 563-82.
32. J.R. Cahoon, W.H. Broughton, and A.R. Kutzak: *Metall. Trans.*, 1971, vol. 2, pp. 1979-83.
33. N.E. Dowling: *ASM Handbook*, vol. 19, *Fatigue and Fracture*, ASM INTERNATIONAL, Materials Park, OH, 1996, pp. 250-62.
34. D.L. Chen, M.C. Chaturvedi, N. Goel, and N.L. Richards: *Int. J. Fatigue*, 1999, vol. 21, pp. 1079-86.
35. M. Klesnil and P. Lukas: *Fatigue of Metallic Materials*, 2nd ed., Elsevier, Amsterdam, 1992.
36. A. Plumtree: *Mater. Sci. Eng. A*, 1997, vols. A234–A236, pp. 636-38.